ELSEVIER

Journal of Nuclear Materials 250 (1997) 131–146

journal of nuclear materials

Morphologies of uranium and uranium–zirconium electrodeposits

Terry C. Totemeier *, Robert D. Mariani

Argonne National Laboratory, P.O. Box 2528, Idaho Falls, ID 83403-2528, USA

Received 19 February 1997; accepted 22 August 1997

Abstract

Uranium and uranium–zirconium electrodeposits produced in the Fuel Cycle Facility at Argonne National Laboratory-West were examined using standard metallurgical techniques. Substantial differences in the morphologies of the two types of deposits were observed. Samples from pure uranium deposits were comprised of chains of uranium crystals with a characteristic rhomboidal shape, while the morphologies of samples from deposits containing zirconium in excess of approximately 0.5 wt% showed more polycrystalline features. Zirconium was found to be present as a second, zirconium metal phase at or very near the uranium–zirconium dendrite surfaces. Higher collection efficiencies and total deposit weights were observed for the uranium–zirconium deposits; this performance increase is likely a result of better mechanical properties exhibited by the uranium–zirconium dendrite morphology. © 1997 Elsevier Science B.V.

1. Introduction

The Argonne National Laboratory (ANL) is currently demonstrating an electrometallurgical process for the treatment of spent nuclear fuel (SNF). The electrometallurgical process was originally developed as part of the integral fast reactor (IFR) program and descriptions of the process as it exists in the context of an IFR fuel cycle have been published [1]. Due to the cancellation of the IFR program, the electrometallurgical process has been redirected towards treatment of spent fuels from the experimental breeder reactor II (EBR-II) [2] and potentially other SNF owned by the US Department of Energy (DOE) [3].

The key element of the treatment process is the electrorefining step. In the electrorefining step, chopped metallic spent fuel slugs contained in steel baskets are placed in a molten eutectic LiCl–KCl electrolyte bath and anodically dissolved. The cathode of the electrochemical cell is a bare steel mandrel, which collects purified uranium. The fission product and actinide contaminants in the spent fuel typically either form chlorides and dissolve into the salt phase or remain as metals, ideally with the cladding hulls in the anode baskets. The fission products and actinides are incorporated into two waste forms, a stainless-steel based metallic form and a glass-bonded zeolite ceramic form [4].

The initial development of SNF electrorefining as it pertains to treatment of EBR-II fuel was carried out at the Argonne-East (ANL-E) site near Chicago, Illinois; the chemical basis and fundamental electrochemistry have been described in papers by Ackerman [5] and Tomczuk et al. [6]. Laboratory-scale tests using simulated SNF at ANL-E demonstrated the feasibility and reliability of the electrorefining process and equipment. The electrorefining technology has been transferred to the Argonne-West site near Idaho Falls, Idaho for a pilot-scale demonstration in the fuel conditioning facility (FCF) hot cells using actual SNF from the EBR-II reactor [7]. As part of the initial start-up activities for the FCF electrorefiner, 31 deposition runs have been made using either pure depleted uranium or an alloy of uranium and 10 wt% zirconium (U–10Zr) as feed material.

Detailed metallurgical examinations were carried out on samples of the uranium deposits from several of the runs to determine the effects of operating parameters on the resulting macro- and micro-morphology of the uranium cathode deposit. These parameters include electrorefining mode, current density, mixing in the salt phase and presence of zirconium in the feed material. This paper presents the results of these examinations and the implications of

* Corresponding author. Tel.: +1-208 533 7458; fax: +1-203 553 7863.

PII S0022-3115(97)00288-2

the observed morphologies for the performance of the deposit in terms of total deposit weight and collection efficiency. The paper also discusses insights that the morphologies of the deposits present in terms of the role of zirconium in the electrodeposition process.

2. Experimental procedures

2.1. FCF electrorefiner description

The FCF electrorefiner is a 0.99 m deep, 1.02 m diameter steel vessel with an operating temperature of 773 K (Fig. 1) located in the FCF purified Ar hot cell. The electrolyte is a molten LiCl–KCl eutectic (41 mol% KCl) with nominally 1.6 mol% UCl_3 dissolved in it; the top of the electrolyte is approximately 0.43 m from the vessel bottom. The electrolyte rests on a pool of molten cadmium whose height is approximately 0.10 m from the vessel bottom. Four circular ports 0.25 m in diameter are used to insert the anodes and cathodes into the electrolyte. As a deposit forms at a rotating cathode, its diameter is limited to 0.25 m by the action of an internal scraper mounted on the inner sidewall of the electrorefiner; the length of the deposit is limited to 0.23 m by a bottom scraper. Any uranium dendrites that are dislodged by the scrapers fall into the cadmium pool and dissolve.

Electrorefiner feedstock consisted of either pure U or U–10Zr alloy as pin pieces or chopped segments (6.4 or 19.1 mm lengths). The feedstock was loaded into perforated, rectangular baskets. Four baskets were assembled together in a cruciform arrangement; the resulting basket assembly was inserted into the electrorefiner to be used as an anode. A solid steel rod 44 or 67 mm in diameter was inserted into the electrorefiner for use as the cathode. Upon insertion, both the cathode and the anode were immersed in the electrolyte to a depth of approximately 0.23 m.

Deposits were produced with a direct current power supply operating under controlled current conditions. The cell voltage (potential difference between anode and cathode) was monitored and compared to a preset maximum cell voltage. The power supply was tripped off when the maximum cell voltage was reached, thus preventing undesirable electrochemical reactions. The electrorefining mode that used the filled basket assembly as anode and steel rod as cathode is referred to as direct transport. In addition to the direct transport mode, the power supply could also be configured with the U-containing Cd pool as the anode and the steel rod as the cathode. This latter configuration is referred to as deposition from the cadmium pool. This electrorefining mode was used to remove U dissolved in the Cd pool.

2.2. Electrorefiner run conditions for deposits examined

The process variables available in the preparation of the deposits included current, cell voltage, electrorefining

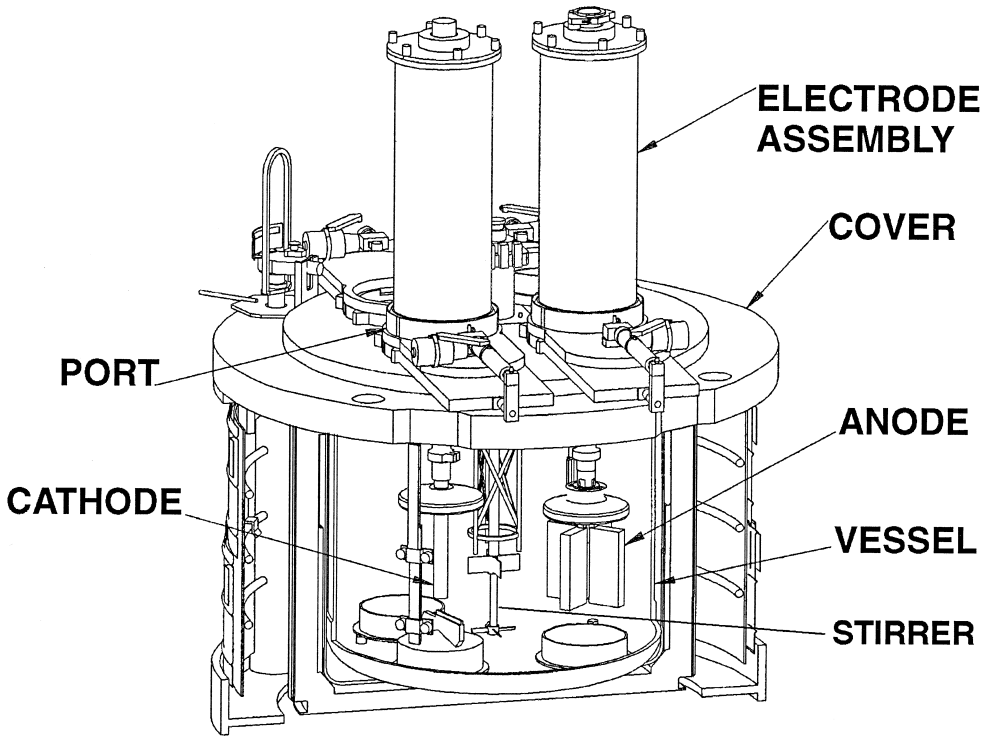

Fig. 1. Schematic diagram of the fuel conditioning facility electrorefiner.

Table 1
Electrorefiner run conditions for deposits examined

	Run/deposit no.						
	3	7	8	25	28	30	31
Conditions							
U concentration in salt (wt%)	4.3	6.4	6.4	6.4	6.4	6.4	6.4
U source (kg)	Cd pool: 14	baskets: 10, Cd pool: 5	Cd pool: 15	baskets: 9.2, Cd pool: 4.8	Cd pool: 9.2	baskets: 8, Cd pool: 8	Cd pool: 10.1
Zr in system?	no	no	no	yes	yes	yes	yes
Electrorefining mode	deposition from Cd pool	direct transport and deposition	deposition from Cd pool	direct transport and deposition	depostion from Cd pool	direct transport and deposition	deposition from Cd pool
Total ampere–hours (A h)	7420	3855/3000	9148	3440/3000	7501	4051/5306	8732
Average current (A)	100	79/158	136	97/138	119	107/160	140
Maximum cell voltage (V)	0.80	1.00/0.80	0.80	0.99/0.76	0.79	1.28/0.79	0.77
Cathode rotation (rpm)	10	20	20	20	20	25	20
Salt mixing (rpm)	25	0	25, 0 after 1700 A h	0	25 (baskets)	25 (baskets)	25 (baskets)
Cd pool mixing (rpm)	25	0	25, 0 after 1700 A h	25	25	25	25
Results							
Total deposit mass (kg)	3.8	6.0	2.9	5.8	10.3	10.8	10.1
Collection efficiency (%)	13	25	9	25	38	33	33
Zr concentration in deposit (%)	0	0	0	150 ppm (dendrite sample)	4.1	2.3	0.2

mode, mixing in the salt and Cd phases, mass of uranium available for transport and cathode diameter. Table 1 shows the run conditions and results for the deposits which were examined; results are given in terms of total deposit mass and collection efficiency. Higher currents generally gave rise to higher cell voltages. When using the U–10Zr alloy feedstock, higher cell voltages favored the combined electrotransport of uranium and zirconium, as discussed in Section 4.2.1.

The electrorefining mode variations utilized in the runs described were deposition from the Cd pool and direct transport followed by deposition from the Cd pool. For runs using the latter mode, relevant data in Table 1 have information related to the direct transport segment separated by a slash from the data related to deposition from the pool. The degree of mixing in the salt and cadmium phases varied due to changes in mixer speed and the use of two different means of stirring. Co-axial salt (flat-blades) and cadmium (downward pitch) stirrers were used for runs 3, 7 and 8; additional salt mixing was provided by rotation of the anode basket assembly as noted in Table 1. The flat-blade salt stirrer was not used during runs 25–31.

As mentioned above, steel cathode mandrels of two diameters were employed: 44 mm (runs 3, 7 and 8) and 67 mm (runs 25–31). The steel cathodes were electrochemically conditioned immediately prior to the runs except for runs 3 and 8. Electrochemical conditioning consisted of configuring the steel mandrel as an anode and the Cd pool as the cathode. Small currents (25 A) are then applied for short times (12 min) to effectively clean the mandrel surface of residues from the previously removed deposit. Deposit removal from the cathode was accomplished by mechanical stripping.

2.3. Sampling and examination procedures

Small samples suitable for examination were removed from deposits in the FCF hot cell using remote manipulators. Clumps of material weighing between 1 and 5 g were broken from representative areas at different locations of the deposit. Samples were removed from the following locations, as shown schematically in Fig. 2, top inside, top outside, middle outside and bottom inside. The specific sampling locations for each deposit are presented in Tables 2 and 3. Note that all of the sample locations are on the periphery of the deposit. The restrictions of hot cell operations did not permit sampling from the interior of the deposit.

The samples were then placed into transfer tubes (Swagelok®-sealed stainless steel) and removed from the hot cell for examination and analysis. As part of preparation for examination, the deposit samples had to be exposed to an air environment, as opposed to the Ar environment of the hot cell. In order to mitigate any potential pyrophoric hazards associated with the U deposits, the transfer tubes containing the samples were carefully opened

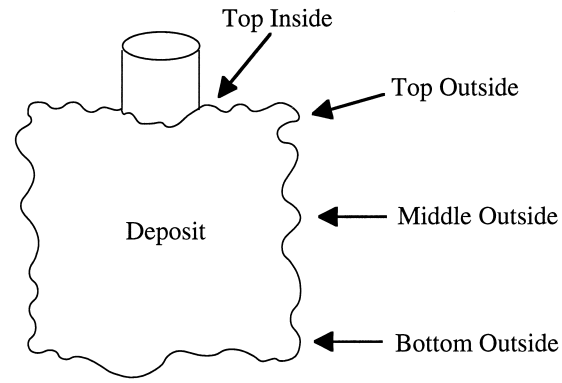

Fig. 2. Deposit sampling locations.

in a fume hood under flowing Ar gas. The Ar gas flow was slowly reduced until only air remained. No visible signs of heating or oxidation were seen. Once the samples had been introduced in the air atmosphere, the residual salt adhering to the U metal was removed. Salt removal was accomplished by ultrasonic cleaning in an ethanol bath punctuated by small additions of distilled water.

Characterization of the cleaned samples was performed using standard metallographic and scanning electron microscopy (SEM) techniques. Metallographic cross-sections of the samples were prepared by mounting an entire piece in either a cold epoxy resin or hot bakelite mount and then grinding the specimen until a suitable section was visible. Both unmounted samples and cross-sections were examined in a ISI SS40 SEM after Pd coating to minimize charging. Semi-quantitative energy-dispersive X-ray analysis (EDS) was performed in the SEM using a Kevex Micro-X 7000 system. In addition, the elemental compositions of the samples were determined by the ANL-W analytical chemistry laboratory using standard chemical techniques.

3. Observed deposit morphologies

3.1. Deposits produced using pure U feedstock

As shown in Table 1, FCF deposits 3, 7 and 8 were prepared using pure U as feed material. Table 2 gives the observed characteristics of the samples from these deposits in terms of morphology, crystal size and presence of interior structure (described below). Surface Zr concentration and presence of Zr phases are also shown in Table 2 for ease of comparison with the U–Zr deposits described in Table 3. The macroscopic morphologies of these three deposits were similar-all showed long dendritic-shaped chains of U crystals. These chains appeared to slump under their own weight. It was clear from examination of the

Table 2
Characteristics of deposit samples examined: pure uranium

Sample	Morphology: crystal size	Overall Zr concentration	Surface Zr concentration	Interior structure	Zr phases in cross-section
Cathode 3					
Top outside	long chain of large rhombic crystals: 0.3–3 mm	not applicable	not applicable	yes	not applicable
Cathode 7					
Middle outside	tangle of fine rhombic crystals: 100–900 μm	not applicable	not applicable	yes	not applicable
Cathode 8					
Top outside	chain of large rhombic crystals: 0.3–3 mm	not applicable	not applicable	yes	not applicable
Middle outside	chains and clumps of larger crystals: 20 μm–2 mm	not applicable	not applicable	yes	not applicable

Table 3
Characteristics of deposit samples examined: uranium–zirconium

Sample	Morphology: crystal in size	Overall Zr concentration	Surface Zr concentration	Interior structure	Zr phases in cross-section
Cathode 25					
Top outside	long chain of rhombic crystals: 0.15–1.5 mm	190 ppm	0.5–1.5 wt%	yes	no
Middle outside	tangle of rhombic crystals: 0.5–2 mm	190 ppm	not available	yes	no
Bottom outside	chains and clumps of rhombic crystals: 80 μm–1.5 mm	< 70 ppm	0.5–1.5 wt%	yes	no
Cathode 28					
Top outside	short chain of large rhombic crystals: 4 mm	3.5 wt%	100 wt%	yes	continuous: 3–10 μm thick
Middle outside	large polycrystalline dendrite	11.5 wt%	100 wt%	no	continuous: 5–20 μm thick
Bottom outside	polycrystalline dendrite	7.3 wt%	29–58 wt%	no	many: 7–20 μm thick
Cathode 30					
Top inside	agglomeration of fine grains: 150–300 μm	2.1 wt%	79–90 wt%	no	many: 2–5 μm thick
Top outside	agglomeration of fine grains: 300–700 μm	0.13 wt%	15–37 wt%	no	few: 0.5 μm thick
Cathode 31					
Top inside	aggregate of blocky crystals: 0.6–1.6 mm	465 ppm	20–67 wt%	no	none
Top outside	large branching polycrystalline dendrite	0.22 wt%	6–24 wt%, blocky protrusions: 60 wt%	not available	not available
Middle outside	large branching polycrystalline dendrite	0.13 wt%	not available	no	none
Bottom outside	tangle of fine rhomboidal crystals	0.46 wt%	10–66 wt%	yes	many: 2–5 μm thick

deposits through the hot cell window that a fairly broad range of crystal sizes were present on each individual deposit. It was not feasible, however, to obtain a proper distribution of crystals sizes and aspect ratios necessary to fully quantify differences between deposits. Hence the descriptions given below are qualitative. At such a level of assessment, the observed morphologies were essentially identical. Fig. 3 is a photograph of deposit 3 taken through the hot cell window. The slumping of the deposit is readily evident. The deposit had a shiny metal color, which correlated with a relatively low residual salt content on the deposit surface. Deposit 7 also showed slumping chains of U crystals, although the crystal size appeared to be slightly smaller. The crystals in deposit 8 were fairly large and more similar to those from deposit 3.

The shapes and arrangements of the U crystals constituting the dendritic chains were revealed by SEM examination. Figs. 4 and 5 show overviews of samples from deposits 3 and 8, respectively. The dendrite-shaped chains of U were comprised of plate-like rhomboidal crystals linked end-to-end. The individual crystals varied in size, both within a single chain and from sample to sample. Fig. 4 shows a chain with relatively large crystals (sizes ranging from approximately 0.3 to 3 mm), while Fig. 5 shows a sample with much finer crystals (sizes ranging from approximately 20 μm to 2 mm). The rhomboidal shape of the crystals suggests that the crystallographic planes observed are not of low index; X-ray diffraction of similar crystals by previous researchers has shown the growth direction to be (310) [8]. Close examination of the crystal surfaces showed them to be essentially featureless. Only a fine oxide-like roughness was visible.

In sharp contrast to their exterior perfection, the interior structure of the crystals was highly complex, as revealed in metallographic cross-sections. Fig. 6 shows a cross-section of a large crystal sampled from deposit 8. It was expected from the exterior views that the cross-sections would show homogeneous, solid, single crystal material, however this was not the case. While no grain boundaries were observed in the crystal, the structure was neither homogeneous nor solid. Instead, the entire crystal was filled with a fairly fine and sometimes oriented structure. Similar structures were observed in all of the larger crystals examined. The structure usually takes the form of interior platelets of U oriented along the long axis of the exterior crystal shape, as is seen at the right-hand side of Fig. 6. It was assumed that the gaps between the U platelets were filled with entrained salt prior to cross-section preparation. The gaps

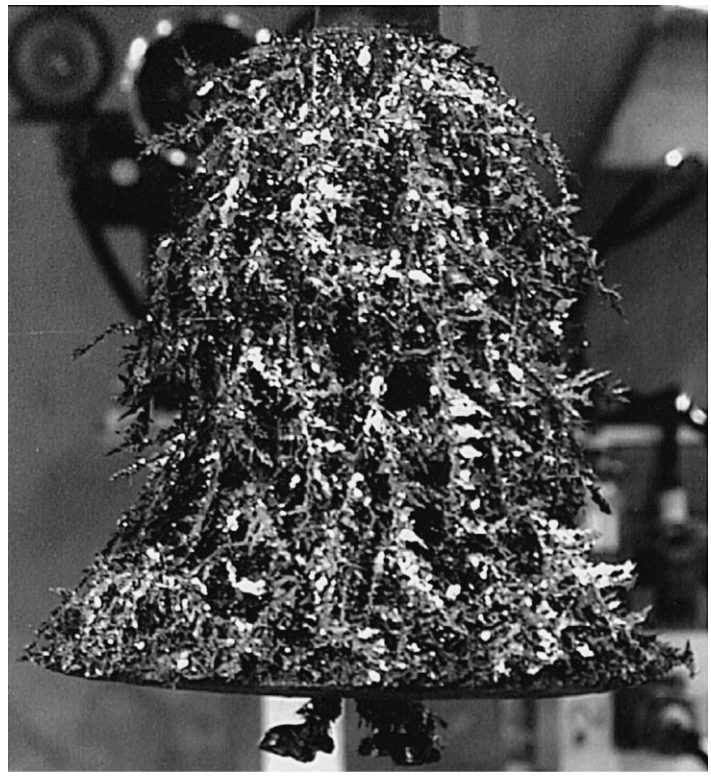

Fig. 3. Macroscopic view of deposit 3. Maximum deposit diameter is 25 cm.

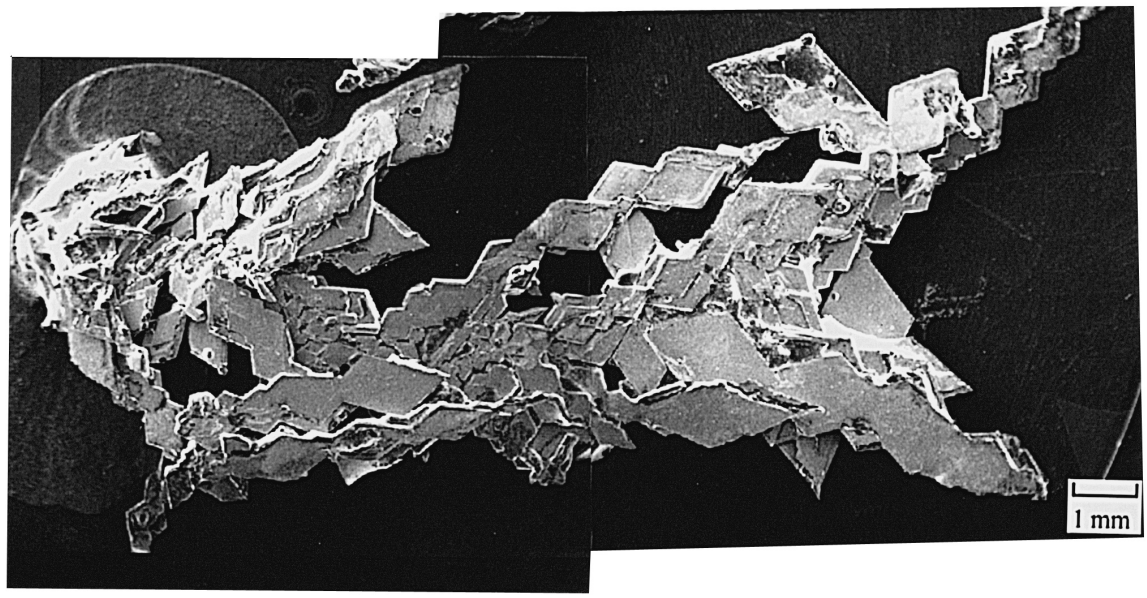

Fig. 4. Overview of a sample from deposit 3 showing chains of linked rhomboidal uranium crystals (10 ×).

Fig. 5. Overview of a sample from deposit 8 showing finer uranium crystals (15 ×).

were not filled with mounting material, and any salt which was present would have been removed by the grinding and polishing procedures. There is no conceivable mechanism for the gaps to be true void space.

Although from the exterior nearly all U crystals appeared to be flawless, one crystal was observed in a deposit 8 sample with features suggesting a sequence for interior structure formation. This crystal is shown in Fig. 7. The faces of the crystal are very regular, with the exception of the one facing the viewer. This face is composed of fine platelets oriented parallel to the top and bottom (as seen in the figure) faces of the crystal. The platelets have a fairly regular spacing. The edges of the face appear to be 'growing over' the platelets to form a smooth exterior surface. Hence a possible growth sequence suggests itself and is depicted in Fig. 8. The original growth is one of several platelets growing parallel to one another from a surface. At some point, the outside platelets change direction and grow over the middle plates, enclosing them in a seemingly perfect crystal. In this process the electrolyte salt is entrained in the crystal. Further discussion of this growth morphology is presented in Section 4.1.

3.2. Deposits produced using U–10Zr feedstock

FCF deposits 25 to 31 were prepared using the U–10Zr alloy as feed material. This alloy constitutes the majority of the EBR-II driver fuel to be treated in the demonstration

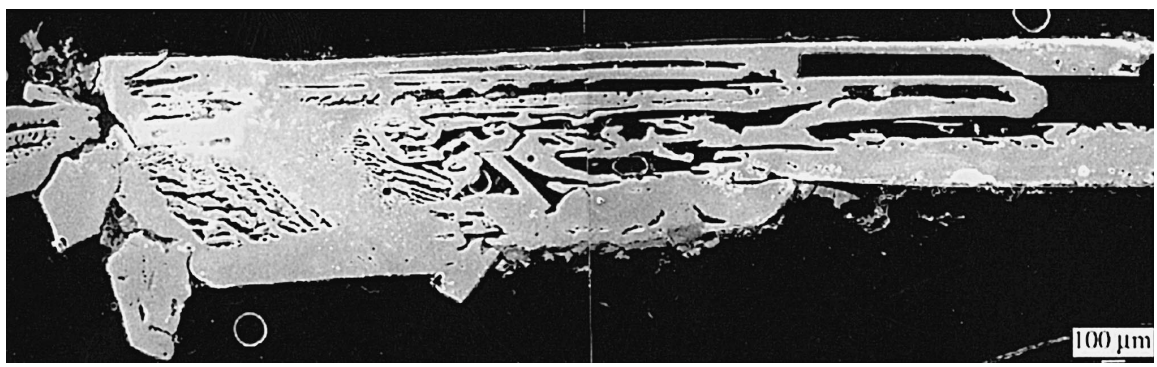

Fig. 6. Cross-section of a large crystal from a deposit 8 sample showing complex internal structure (40 ×).

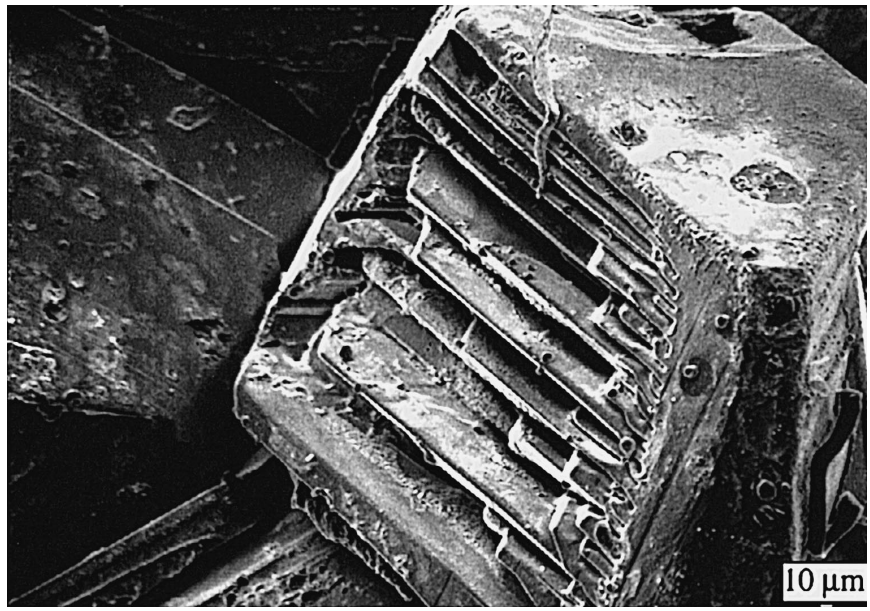

Fig. 7. Incomplete crystal observed in deposit 8 sample (170 ×).

project. The actual SNF, of course, also contains numerous fission product contaminants, but no attempts were made to simulate their presence. Previous electrorefining experience with U–Zr alloys in the laboratory-scale electrorefiner at ANL-E suggested that a different deposit morphology would be observed for U–Zr feedstock compared to pure U. Due to the similarity in redox potentials for U and Zr, under normal operating conditions (a cell voltage of approximately 0.7 V) some Zr deposits at the cathode along with U. A true separation of U and Zr is possible using lower cell voltages (less than approximately 0.4 V) [9].

Table 3 presents the observed characteristics of the U–Zr samples in terms of morphology, crystal size, surface Zr concentration, presence of interior structure and presence of Zr phases. Deposit 25 was the first to be made using U–Zr as feedstock. Due to the low activity of Zr in the electrorefining system at that time, very little was transferred to the cathode. The Zr concentration in the metallic deposit measured by analytical chemistry of dendrite samples was 150 ppm. The morphology of deposit 25 strongly resembled that of the previous deposits made using pure U as feed material. Apparently the presence of Zr at low activity did not affect the deposition process.

The U–10Zr alloy continued to be used as anode feedstock and significant (approximately 1 wt% and above)

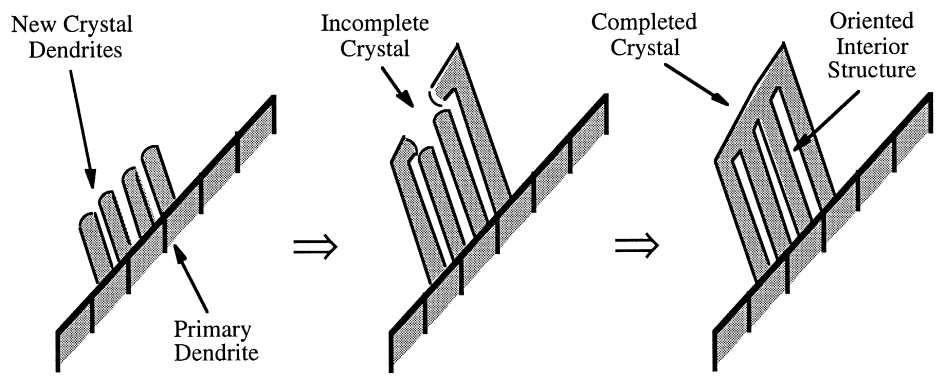

Fig. 8. Schematic diagram of possible crystal growth sequence.

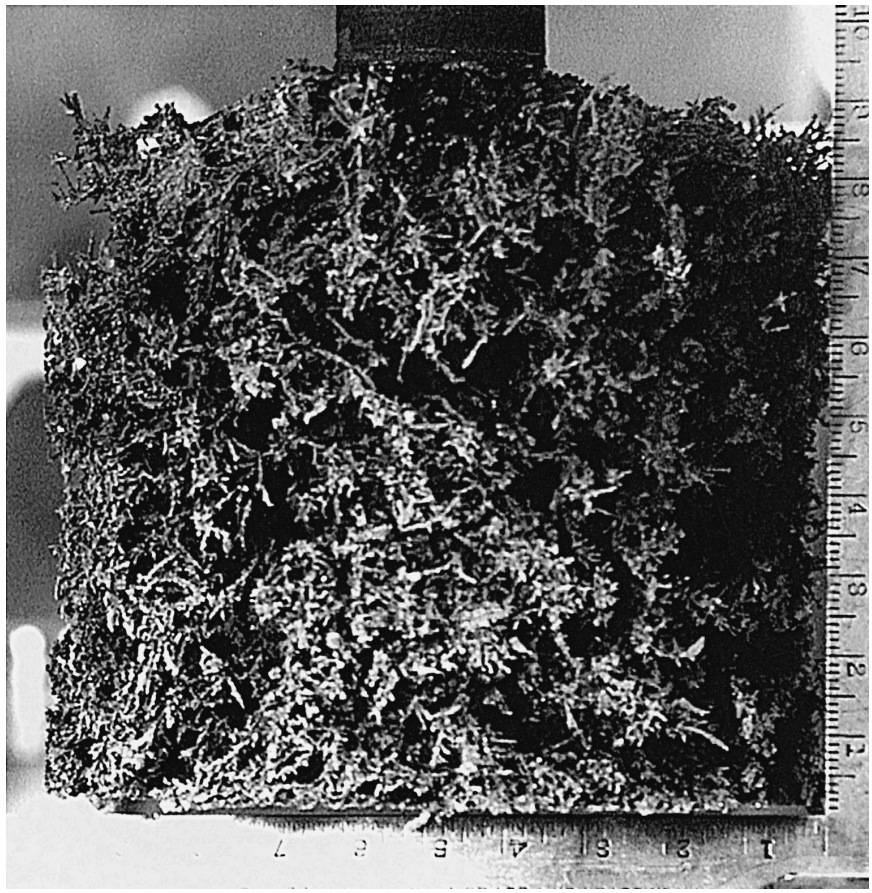

Fig. 9. Macroscopic view of deposit 30. Maximum deposit diameter is 25 cm.

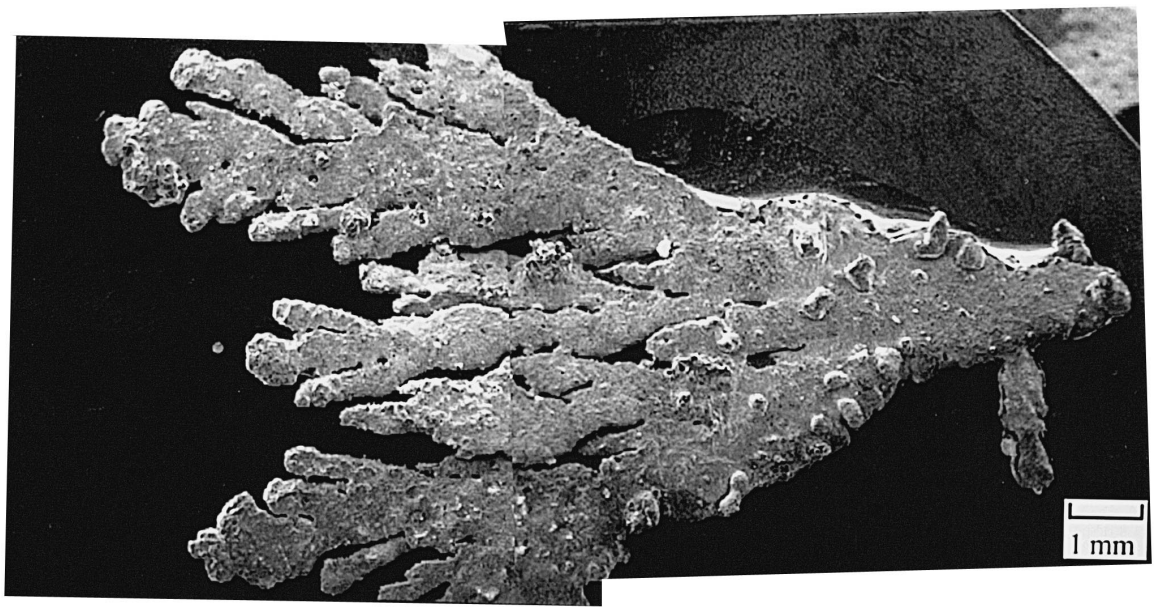

Fig. 10. Overview of a leaf-shaped dendrite from deposit 30 (10 ×).

amounts of Zr was present in deposits 27 to 31. The macroscopic morphologies observed for these deposits were similar and very different from the morphologies observed for the previous deposits which contained little or no Zr. A typical macroscopic morphology for Zr-containing deposits is shown in Fig. 9 for deposit 30. This deposit was still very dendritic, however the dendrites did not slump, in contrast to the pure U deposits. The right cylindrical shape of the deposit is a result of shaping by deposit rotation past fixed scrapers. The mass of deposit 30 was considerably higher than that of deposit 3 (Fig. 3), 10.8 kg compared to 3.8 kg. The color of this and other U–Zr deposits was a dull gray; no shiny metallic features were visible.

The sample morphologies as viewed in the SEM were varied, but could generally be described as dendrite-shaped agglomerations of fine U grains, i.e. polycrystalline material. The more specific morphological types observed include leaf-like dendrite shapes, loose agglomerations of blocky fine crystals, aggregates of fine irregular grains and also tangles of fine rhomboidal crystals similar to those observed in pure U deposits. No chains of large crystals were observed, however. A example of a typical morphology is shown in Fig. 10, which is a leaf-shaped dendrite from deposit 30. Close examination of the surfaces of the sample surfaces tended to reveal either blocky features reminiscent of intergranular fracture surfaces or fine-scale steps and ledges which appeared to be crystallographic in origin. Fig. 11 shows a higher magnification view of the surface of the sample in Fig. 10.

The concentration of Zr on the surfaces of the U–Zr deposit samples was semi-quantitatively evaluated using EDS. A wide variation of Zr concentrations, from approximately 6 to 100 wt%, was found from sample to sample and also within single samples. There appeared to be no correlation of surface feature type or size with surface Zr concentration.

The internal structure of 'typical' polycrystalline agglomerate dendrites reflected their external structure. Light microscopy examinations showed the dendrites to be polycrystalline; relatively fine grains were readily apparent on as-polished samples due to oxidation contrast. No extensive internal structure was observed, however porosity was still present, as shown in Fig. 12a. The porosity tended to be slightly aligned along the long axes of the dendrites.

A second phase along the cross-section edges was observed for some of the U–Zr samples. This phase was bright (unoxidized, unlike the bulk U) in the light microscope and dark in the SEM (due to atomic number contrast). Fig. 12b is a closer view of Fig. 12a showing this phase. EDS analysis of the phase showed only a Zr peak, hence this phase was identified as α-phase Zr metal. The Zr phase was not observed in the interior of the cross-section, although occasionally a very thin, irregular line (approximately 0.5 μm thick) of the phase was found just to the interior of the cross-section edge. EDS analysis of the bulk, bright phase in the SEM showed only U peaks. No Zr was ever found in any form other than the dark phase, however it is possible that Zr could be present in quantities less than the detection limit of the EDS system used, approximately 0.5 wt%.

The Zr phase was also found on the other morphological forms observed for the U–Zr deposits, most notably the

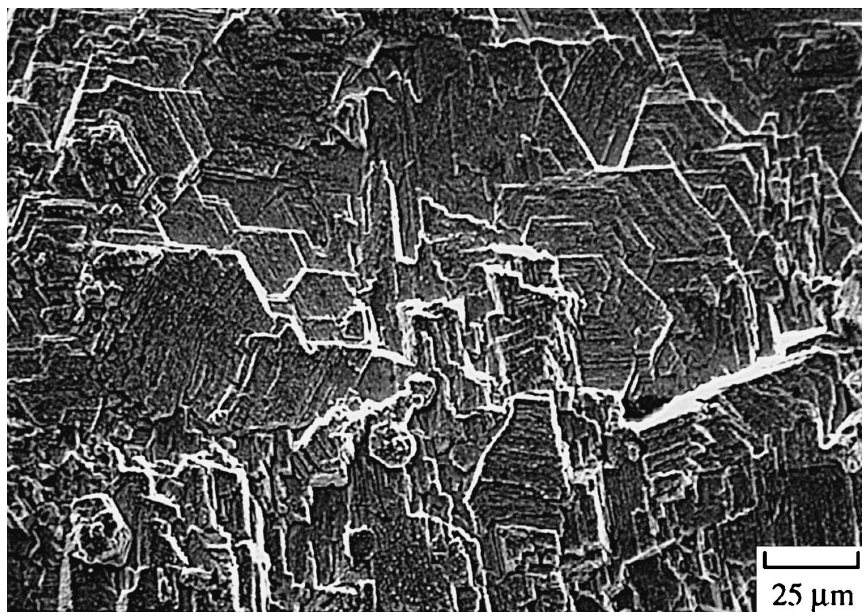

Fig. 11. Close-up of dendrite surface showing crystallographic steps and ledges (500 ×).

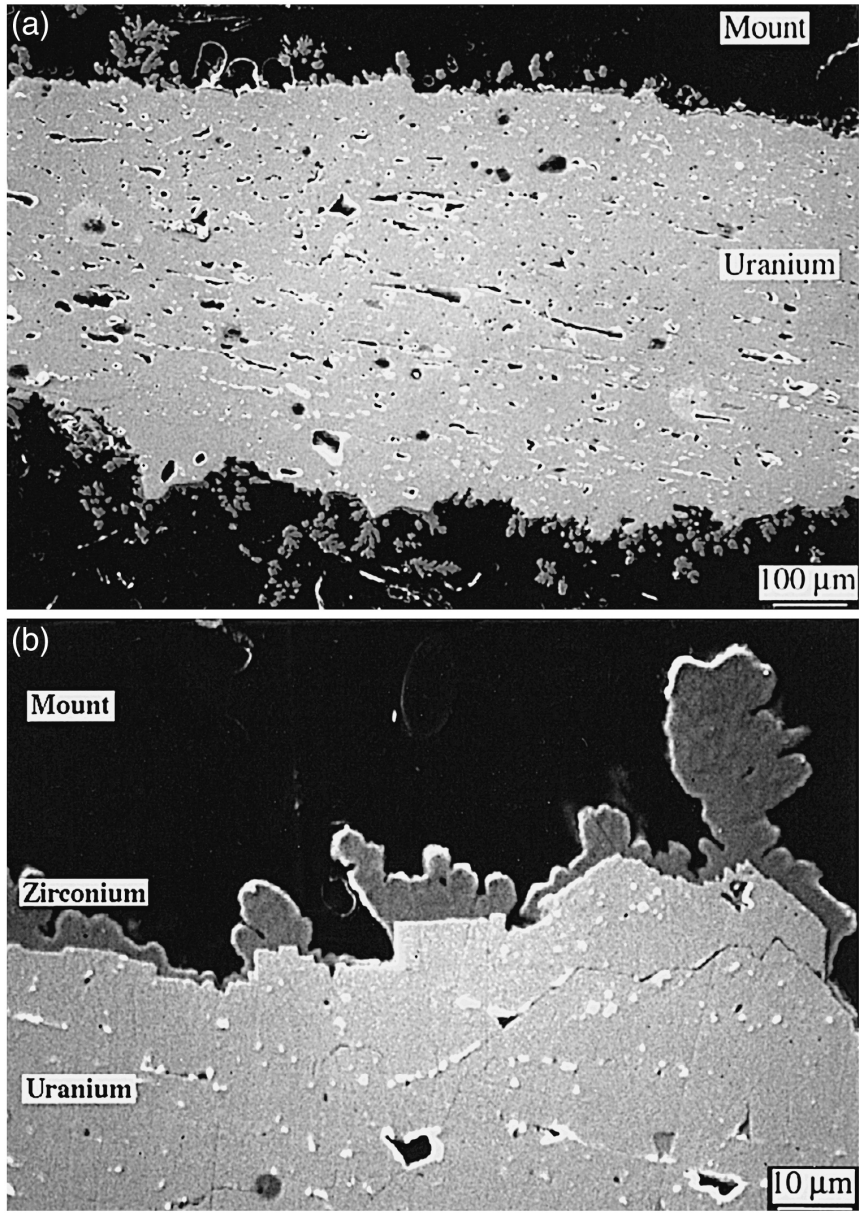

Fig. 12. (a) Cross-section of a polycrystalline dendrite from Deposit 28 showing irregular porosity (100 ×). (b) Higher magnification view showing zirconium metal phase at the dendrite surface (1000 ×).

rhomboidal crystals. The internal structure of these crystals was identical to that found for the pure U crystals-platelets oriented along the long axis of the crystal. On the surfaces of the crystals, however, a layer of Zr phase identical to that shown in Fig. 12b was present. No Zr phase was present on any of the internal surfaces.

A number of samples from deposits 30 and 31 were taken at different locations in an attempt to observe systematic variations in sample morphology, surface Zr content, or presence of Zr phases with sample location. Of particular interest were variations with radial distance from the mandrel. Inspection of Table 2 shows that there is no discernible trend present. Also, little correlation was found between the Zr surface concentrations, the presence of Zr phases in the cross-sections and the overall morphologies. Some samples with more crystalline features, such as the deposit 31 bottom outside sample, had larger quantities of Zr in evidence than other samples showing few or very fine features, such as the deposit 31 top and middle outside samples.

4. Discussion

4.1. Morphology of pure U deposits

The crystallographic, dendritic morphology of the pure U deposits is identical to that observed by previous researchers. Development of uranium electrorefining in molten chloride salts began in earnest in the late 1950s and 1960s by researchers at Argonne National Laboratory [8], the US Bureau of Mines [10,11] and in France [12,13]. Formation of dendrites composed of chains of linked rhomboidal crystals was always observed. Marzano and Noland [8] performed Laue X-ray diffraction on the crystals and determined that the preferred growth direction was (310). In fact, it appears to be very difficult to obtain U deposits which are not dendritic, as found by workers at Argonne trying to deposit uniform layers [14].

Some studies report a dependence of crystal size on initial current density. Both Cattoir and Sullivan [11] and Marzano and Noland [8] found thinner, higher aspect ratio dendrites at higher current densities. The initial current densities investigated by these researchers encompass those used in the present study. Initial current densities used in the production of FCF deposits were approximately 2,000 A/m^2; those investigated by Cattoir and Sullivan [11] (who examined the widest range of initial current densities) varied from 300 to 20 000 A/m^2. There was no discernible effect of varying average current on crystal size or morphology in the present study. Due to the changing deposit surface area during deposition, it is difficult to assess the differences in true current densities under which the samples examined were produced. However, the possible changes in current densities produced by the factor of two variations in average current for the FCF deposits are much less than the order of magnitude variations needed to significantly affect deposit morphology in previous works. Other parameters, such as mixing and deposition mode, also did not appear to measurably affect the morphologies of the deposit samples examined.

One aspect of the pure U crystal morphology which has not been previously reported is the complex internal structure of the crystals. A possible sequence for formation of the structure was presented in Section 3.1. Electrodeposition theory as it is currently understood does not provide an explanation for why individual dendrites would grow together to form apparently perfect larger crystals.

4.2. The role of Zr in electrodeposition

It is clear from the results presented in Section 3 that deposits containing quantities of Zr in excess of approximately 0.5 wt% have morphologies which are significantly different from deposits containing no or very little Zr. The deposits which contain Zr in higher levels have a more fine-grained, polycrystalline character than pure U deposits, which are composed nearly exclusively of relatively large, rhomboidal crystals. In addition, the Zr-containing deposits show the presence of a second phase of pure Zr metal; this phase is observed only at or very near deposit surfaces. The morphology change appears to be linked to Zr presence in the deposit and not just Zr presence in the electrorefining system. Deposit 25 is a good example of a deposit for which Zr was present in the system but not in the deposit. The average Zr content of deposit 25 dendrite samples, determined by analytical chemistry, was approximately 150 ppm. The morphology of the dendrites examined strongly resembled that of pure U deposits.

The obvious issue to be considered is the mechanism by which the presence of Zr in the deposit changes the growth morphology of uranium electrodeposition. The issue breaks down into two fundamental questions. First, why and how does Zr transport from the anode feed to the deposit, and second, how does the presence of Zr change the growth morphology?

4.2.1. Zr oxidation and deposition

A full discussion of Zr transport in the FCF electrorefiner is outside the scope of the present work and the reader is referred to articles which discuss the chemical basis for electrorefining of spent nuclear fuel [5,6]. A simplified discussion is presented below.

In order for Zr to deposit at the cathode, it must exist in the salt (as $ZrCl_2$) in the immediate vicinity of the cathode surface. Since UCl_3 is more stable than $ZrCl_2$, any Zr^{2+} at the cathode will be preferentially reduced to the metal compared to U^{3+}. At sufficiently high cell voltages, Zr^{2+} ions are produced in the salt by electrochemical oxidation of Zr metal at the anode. Zr metal is originally present as part of the U–10Zr alloy feedstock and also can be present in the Cd pool incidental to the electrorefining process. Following oxidation, the Zr^{2+} ions are transported to the vicinity of the cathode, primarily via convection (stirring of the salt). Once they reach the cathode they will deposit.

The amount of Zr oxidized, expressed as a fraction of the total cell current, is predicted to vary over the course of an electrorefining run. The initial amount of Zr oxidized is low due to the difference in equilibrium cell potentials for Zr and U and the lower activity of Zr in the U–10Zr alloy compared to U. As the run progresses and U is oxidized from the alloy, the activity of Zr increases relative to the activity of U. The increasing overpotential at the anode provides an additional increase in Zr current. These two factors result in an increasing Zr oxidation current over the course of a run. Because the Zr deposition rate is directly dependent on the oxidation rate, a similar variance in Zr deposition rate is predicted to occur.

The observed location of Zr in the cross-sections of deposit samples, however, does not entirely fit with predictions of when Zr is deposited. The inconsistency is that Zr is only observed at or near the surfaces of deposits and not at all in the interior, contrary to the prediction of Zr deposition throughout the run. The statement that Zr is not

observed in the interior must be predicated with knowledge of the detection limits of the EDS system which was used for microchemical analysis, which are on the order of 0.5 wt%. Zr could therefore be present in undetectable impurity levels throughout the deposit.

Given that information, a few ways exist to reconcile prediction and observation. The first possibility is that Zr is present throughout the deposit at the levels predicted: these might be undetectable in the centers of dendrites (the first material of the sample to deposit). If this were true, however, a gradation in Zr concentration through the thickness of the deposit corresponding to the variation in Zr current fraction may be expected to exist. Zr concentrations would be high (and therefore detectable) at the surface and gradually decrease until the limit of detection was reached. Such a concentration gradient was not observed; Zr was only found in discrete phases at the surface.

A second explanation, one more consistent with observations, is that Zr atoms are sufficiently mobile on the electrodeposited U surface to always be present at the surface and not be incorporated into the bulk metal. Two observations support this hypothesis. First, Zr has very limited solid solubility in α-phase U metal at the deposition temperature, less than 0.2 wt% [15]. Levels of Zr greater than the solubility limit would be rejected by the growing U lattice. Second, high diffusion coefficients can be achieved on the surfaces of growing electrodeposited metals due to a high vacancy concentration [16]. Rapid solid state diffusion is the only requirement to maintain the 'equilibrium' state of Zr and U separation into two phases. This requirement is considered achievable at 773 K under conditions of high vacancy concentration on the dendrite surface and along the U–Zr interface. Phases with compositions corresponding to the UZr_2 intermetallic were not observed.

4.2.2. Zr effects on growth processes

The question of how the presence of Zr atoms during the electrodeposition of U changes the morphology of the deposited U is difficult to answer using the experimental information available. The deposits examined were not created under carefully controlled conditions that might enable determination of the influences of specific variables, but rather as part of a large-scale process occurring remotely in a hot cell. The known fact is that deposits which contain significant quantities of Zr possess more polycrystalline attributes than pure U deposits. No other variable yet identified exerts such a strong influence on morphology.

Comparison of this fact with the available literature on electrodeposition suggests that Zr may be acting as an inhibitor in this system [17,18]. The action of an inhibitor is to promote denser and finer-grained deposits by occupying active surface sites on the growing lattice. An inhibitor can be any species which hinders the cathodic process present at the electrode surface, in the double layer, or in the diffusion zone. As an example, organic molecules are commonly used as inhibitors in electrodeposition from aqueous solutions to promote smooth deposits [17]. The Zr ion would be a strong candidate for an inhibitor because it is favorably reduced in comparison with uranium. It is therefore easily envisioned occupying active surface sites, forcing uranium atoms to nucleate new grains rather than continue to grow along preferred crystallographic planes.

The observed location of Zr in U–Zr deposits, especially viewed in relationship to the morphology of the sample, does not entirely support this hypothesis. Although deposits having Zr definitely appear more dense and tend to show more polycrystallinity, an example exists which appears to be in direct contradiction to this trend. The top outside sample from deposit 28 was a short chain of large rhomboidal crystals which contained 3.5 wt% Zr. The Zr was present as a 3–10 μm thick continuous layer on the outside surfaces of the crystals. If Zr acted as an inhibitor, any crystalline areas observed in U–Zr deposits would be expected to be associated with locally very low Zr concentrations; however it is also possible that the Zr layer was deposited at the end of the run after the U crystals had stopped growing (being fully formed), providing sort of an 'overcoat'. This example demonstrates that considerably more work is required to determine the deposition mechanisms operative in this system.

4.3. Performance implications of morphologies

The performance implications of the U–Zr deposit morphology in comparison with the pure U deposit morphology are fairly clear: better performance in terms of total deposit weight and collection efficiency is obtained for the U–Zr deposits. The total weights achieved for the pure U deposits were never greater than 8 kg; 10 kg weights were routinely obtained for U–Zr deposits. Collection efficiency is defined as the ratio of the actual amount of uranium deposited to the theoretical maximum able to deposit based on time-integrated current (A h). The collection efficiencies for the pure U deposits examined varied from 9 to 25%, while the collection efficiencies for the U–Zr deposits varied from 33 to 38%. The variation in collection efficiency with duration of run in ampere–hours is shown in Fig. 13 for all pure U and U–Zr deposits (not only those with detailed examinations). These deposits were produced under a wide range of conditions, and no other variable shows as much effect on collection efficiency as does the presence or absence of Zr.

Such a performance improvement would be expected based on simple mechanical considerations of the two morphology types. The limits on deposit performance are set by the ability of the dendrites to withstand the process of shaping by rotation past the scrapers. As the outermost dendrites contact the scrapers, torsional shear forces are placed on the deposit which can lead to separation of dendrites either from themselves or the steel mandrel.

Dendrites so separated fall into the Cd pool at the bottom of the electrorefiner, where they can be later recovered by using the Cd pool as an anode. Separation of dendrites results in lowered collection efficiency; indeed this is likely the main reason collection efficiencies closer to 100% are not obtained in the FCF electrorefiner. Very high collection efficiencies have been reported by previous researchers [8,10,11,13,19]. The deposits collected in the previous studies were not rotated and subjected to stress in the form of scraper contact. The growing weight of the deposit itself will also provide stress to result in dendrite separation. The entire deposit mass, up to 11 kg, must be supported by the bond between the uranium deposit and the steel mandrel and the dendrites must resist slumping under their own weight to avoid the bottom scraper.

Hence a few desirable mechanical properties are identified: (i) resistance to deformation of the dendrite chains, especially with respect to bending stresses, (ii) resistance to failure by separation and (iii) good bonding between the deposit and the steel mandrel substrate (this may also be a chemical attribute). Comparison of the pure U and U–Zr deposit morphologies leads to the conclusion that the U–Zr deposits are expected to show better performance for the above measures. The dendrites for the pure U deposits tend to be composed of chains of single crystals. The resistance of the chains to bending and separation will be low because of the weak link between adjacent crystals (Fig. 4). Handling experience with samples of these deposits supports this conclusion; the chains are easily broken with tweezers by bending at the links. The more polycrystalline nature of the U–Zr deposits and more continuous nature of the dendrites suggest that they would have higher resistance to deformation, a position which is also supported by sample handling experience. The U–Zr samples tended to be much more difficult to pull apart. Due to the difficulty of obtaining suitable samples, a comparison of the deposit–substrate interface for the two types of deposits has not been performed, so no conclusions may be reached about the relative strengths of the deposit–mandrel bonds.

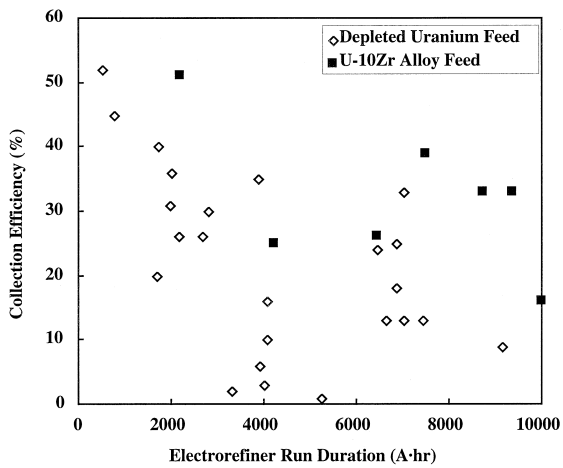

Fig. 13. Variation of collection efficiency with run duration for all U and U–Zr deposits.

An additional aspect of deposit performance is the degree of separation of U from fission products, or 'decontamination,' which is achieved in the electrorefining process. A high degree of decontamination is required if the separated uranium is to be re-used as reactor fuel or stored as low level waste. In this respect the presence of Zr in cathode deposits is undesirable, because Zr in spent fuel is present as a radioactive fission product (Zr-93) as well as an intentional alloying addition. From the standpoint of reuse as fuel any isotopes of Zr are undesirable. A trade-off therefore appears to exist between good mechanical performance conferred by the presence of Zr set against the need for decontamination. Further understanding of the deposition process and the role of Zr in deposition is needed to obtain desirable morphologies while minimizing Zr present in the deposit.

5. Conclusions

Examinations of pure U and U–Zr electrodeposits produced in the FCF electrorefiner at ANL-W were performed and substantial differences were observed in the morphologies of the two types of deposits. Samples from pure U deposits were comprised of chains of U crystals with a characteristic rhomboidal shape and complex internal porosity structure. The morphologies of samples from deposits containing Zr in excess of approximately 0.5 wt% showed more polycrystalline features. While some samples from U–Zr deposits still exhibited the crystalline morphology of the pure U deposits, most were comprised of polycrystalline dendrites or aggregates of fine grains. Zr was found to be present as a second, Zr metal phase at or very near the surfaces of the dendrites examined.

The implications of the observed morphologies were considered. The differences in morphologies of the pure U and U–Zr deposits suggest that Zr may be acting as an inhibitor for U electrodeposition, however the evidence supporting this hypothesis was not conclusive and in one instance was in apparent contradiction. The change in morphology due to Zr addition suggests that the better performance of the U–Zr deposits is likely a result of better mechanical properties of the U–Zr dendrites.

Acknowledgements

The authors wish to acknowledge the following people for assistance with this work: E.L. Wood, K. Nissen, N. Bomono, R. Benedict, D.C. Crawford and J.R. Krsul. This work was supported by the US Department of Energy,

Reactor Systems, Development and Technology, under contract W-31-109-Eng-38.

References

[1] J.J. Laidler, J.E. Battles, W.E. Miller, J.P. Ackerman, E.L. Carls, Prog. Nucl. Energy 31 (1997) 131.
[2] K.M. Goff, R.W. Benedict, D. Levinskas, Proc. Topical Meeting on DOE Spent Nuclear Fuel: Challenges and Initiatives, Salt Lake City, UT, Dec. 13–16, ANS, La Grange Park, IL, 1994.
[3] J.J. Laidler, Proc. Topical Meeting on DOE Spent Nuclear Fuel: Challenges and Initiatives, Salt Lake City, UT, Dec. 13–16, ANS, La Grange Park, IL, 1994.
[4] J.P. Ackerman, T.R. Johnson, L.S.H. Chow, E.R. Carls, W.H. Hannum, J.J. Laidler, Prog. Nucl. Energy 31 (1997) 141.
[5] J.P. Ackerman, Ind. Eng. Chem. Res. 29 (1991) 140.
[6] Z. Tomczuk, J.P. Ackerman, R.D. Wolson, W.E. Miller, J. Electrochem. Soc. 139 (1992) 3523.
[7] K.M. Goff, R.D. Mariani, D. Vaden, N.L. Bomono, S.S. Cunningham, Proc. Embedded Topical Meeting on DOE Spent Nuclear Fuel and Fissile Material Management, Reno, NV, June 16–20, ANS, La Grange Park, IL, 1996.
[8] C. Marzano, R.A. Noland, The Electrolytic Refining of Uranium, Argonne National Laboratory Report ANL-5102, 1953.
[9] E.C. Gay, W.E. Miller, Proc. Topical Meeting on DOE Spent Nuclear Fuel: Challenges and Initiatives, Salt Lake City, UT, Dec. 13–16, ANS, La Grange Park, IL, 1994.
[10] R.E. Campbell, T.A. Sullivan, Electrorefining Uranium in a Chloride Electrolyte, US Bureau of Mines Report 6624, 1964.
[11] F.R. Cattoir, T.A. Sullivan, Molten-Salt Electrorefining of Uranium, US Bureau of Mines Report 6507, 1964.
[12] G. Boisde, G. Chauvin, H. Coriou, J. Hure, Electrochim. Acta 5 (1961) 54.
[13] G. Chauvin, H. Coriou, P. Jabot, A. Laroche, J. Nucl. Mater. 11 (1964) 183.
[14] S.L. Marshall, L. Redey, G.F. Vandegrift, D.R. Vissers, Electroformation of Uranium Hemispherical Shells, Argonne National Laboratory Report ANL-89/26, 1989.
[15] M.E. Kassner, D.E. Peterson (Eds.), Phase Diagrams of Binary Actinide Alloys, ASM International, Materials Park, OH, 1995.
[16] J.O.M. Bockris, A.K.N. Reddy, Modern Electrochemistry, vol. 2, Plenum, New York, 1970.
[17] R. Winand, Electrochim. Acta 39 (1994) 1091.
[18] G. Wranglen, Electrochim. Acta 2 (1960) 130.
[19] J.E. Antill, D.S. Butler, E. Barnes, in: H.M. Finneston, J.P. Howe (Eds.), Progress in Nuclear Energy, ser. V, Metallurgy and Fuels, Pergamon, New York, 1959, p. 3.